Nonequilibrium magma degassing: Results from modeling of the ca. 1340 A.D. eruption of Mono Craters, California

Helge M. Gonnermann [a,*], Michael Manga [b,1]

[a] *Department of Earth and Planetary Sciences, Harvard University, 20 Oxford Street, MA 02138, USA*
[b] *Department of Earth and Planetary Science, University of California, 307 McCone Hall, Berkeley, CA 94720-4767, USA*

Abstract

We present results from a numerical conduit model of nonequilibrium magma degassing. We show that CO_2/H_2O concentration ratios in pyroclastic obsidian from the ca. 1340 A.D. Mono Craters eruption may record nonequilibrium degassing during magma ascent. Our results also indicate that permeability-controlled, open-system gas loss is consistent with obsidian formation and promotes nonequilibrium degassing at shallow depths. Because of the low diffusivity of CO_2 relative to H_2O, we find that CO_2 concentrations can remain above equilibrium during magma ascent. To reproduce Mono Craters volatile concentrations, our model does not require volatile supersaturation, or an exsolved gas phase, prior to magma eruption. We estimate magmatic volatile contents of approximately 400 ppm CO_2 and 4.6 wt.% H_2O. However, nonequilibrium is contingent upon low rates of bubble nucleation to shallow depths, so that average bubble number densities are of order 10^{11} m^{-3} during most of the magma ascent. If bubble number densities during ascent of the Mono Craters magma were greater than 1011 m^{-3}, degassing was in equilibrium and a CO_2-rich vapor buffer is required to reproduce observed CO_2/H_2O concentration ratios.
© 2005 Elsevier B.V. All rights reserved.

1. Introduction

The concentration of CO_2 and H_2O in volcanic glasses is one of the few available measurements that is directly related to syneruptive magma dynamics. The solubility of volatiles, predominantly H_2O and CO_2, in silicate melt is pressure dependent. Ascent-driven decompression causes bubble nucleation and growth by volatile exsolution and by expansion of

---

* Corresponding author. Tel.: +1 617 496 6796; fax: +1 617 495 8839.
  E-mail addresses: gonnermann@eps.harvard.edu
(H.M. Gonnermann), manga@seismo.berkeley.edu (M. Manga).
  [1] Tel.: +1 510 643 8532; fax: +1 510 643 9980.

already exsolved vapor (e.g., [1]). If no gas escapes from the growing bubbles, then the melt with dissolved plus exsolved volatiles in bubbles form a closed system. During ascent the magma can attain large vesicularity and/or overpressure within bubbles (Fig. 1). In the open-system case, gas can escape from the bubbles during magma ascent and vesicularity, as well as overpressure, may remain small (Fig. 1). Consequently, degassing is thought to be one of the key processes in determining explosive versus effusive eruptive behavior (e.g., [2–8]).

Obsidian is dense, essentially non-vesicular, volcanic glass. While parental magmas are thought to be saturated with dissolved volatiles, the low volatile content and the absence of vesicularity requires open-system degassing for the formation of obsidian. Obsidian is most abundant in effusive lavas, but it is also found in tephra from explosive eruptions. Pyroclastic obsidian from the ca. 1340 A.D. Plinian eruption of Mono Craters, California contains measurable quantities of CO_2 and H_2O, and is thought to record magmatic volatile contents at the time of fragmentation and quenching [9]. During ascent-driven decompression CO_2 and H_2O solubilities decrease (Fig. 2). However, because volatile solubility also depends on the vapor-phase composition, Newman and coworkers [9] interpreted the Mono Craters

Fig. 2. Equilibrium concentrations of CO_2 and H_2O that are dissolved in silicic melt at a temperature of 900 °C [28]. Each dotted line is a pressure isopleth and each CO_2 and H_2O concentration pair on a given isopleth corresponds to a specific vapor-phase composition. At any given pressure, an increase in CO_2 content of the vapor phase results in an increase in CO_2 solubility and a decrease in H_2O solubility. At the same time, solubilities of both CO_2 and H_2O decrease with decreasing pressure, resulting in volatile exsolution during ascent-driven decompression. Also shown are measured concentrations in Mono Craters obsidian samples [9].

CO_2/H_2O concentration ratios data to be the result of closed-system degassing in the presence of a buffering CO_2-rich vapor phase. Because obsidian is essentially degassed and vesicle-free, closed-system degassing represents a paradox in terms of obsidian formation [9]. Subsequently, Rust et al. [10], motivated by textural evidence of brittle deformational processes in obsidian samples, suggested that degassing and obsidian formation was the consequence of magma autobrecciation by shear along the conduit walls [11,12]. However, in their model the elevated CO_2/H_2O concentration ratios of the Mono Craters samples still require the presence of a buffering CO_2-rich vapor phase. Both of these models [9,10] imply a high CO_2 abundance in the parental magma, with CO_2 saturation at pressures of approximately 1400 MPa, possibly consistent with a deep-crustal basalt system that released CO_2 into the shallower Mono Craters magma prior to eruption (e.g., [16,17]). Because of the implications for pre-eruptive magmatic gas content (e.g., [13–17]), eruption triggering (e.g., [19]), as well as eruption dynamics (e.g., [20] and references therein), it is important to test the validity of concentration estimates based on equilibrium degassing models [18].

The goal of this work is to test if a CO_2-rich vapor phase is required to explain the measured CO_2/H_2O concentration ratios. We present results from a numerical conduit model of nonequilibrium, closed-system
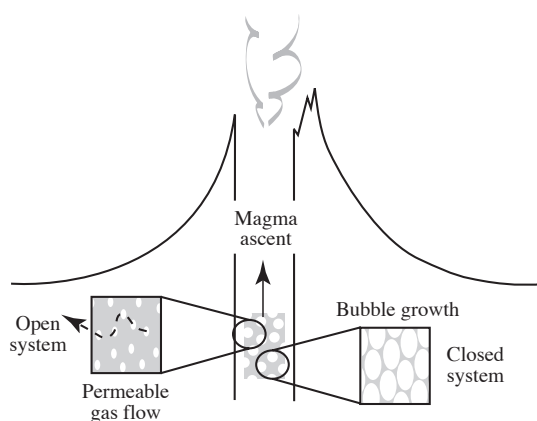

Fig. 1. Schematic illustration of open- vs. closed-system degassing during magma ascent in a volcanic conduit. Pressure decreases as magma ascends. During open-system degassing (left) permeable gas flow through the porous magma allows volatiles to be lost from the ascending magma. Consequently, bubbles remain small. In the case of closed-system degassing (right); mass flux of volatiles into the bubble and decompression-driven expansion of exsolved volatiles results in bubble growth.
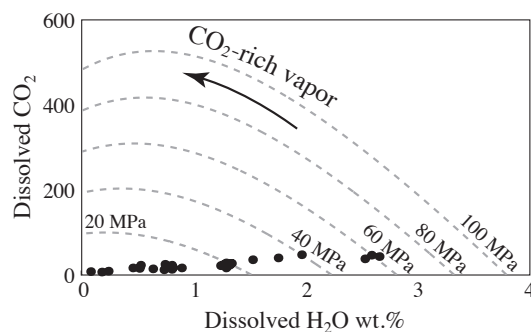
and permeability-controlled open-system degassing of CO_2 and H_2O. As already pointed out by Watson [21], diffusive fractionation of CO_2 and H_2O are likely, because the diffusivity of CO_2 in the melt is approximately one order of magnitude smaller than that of H_2O under relevant pressures and temperatures. Accordingly, we find that volatile concentrations of Mono Craters obsidian samples can be explained by nonequilibrium degassing.

2. The model

We model volatile exsolution (CO_2 and H_2O) and ensuing bubble growth during magma ascent at constant mass flux and invariant properties with respect to conduit radius. The bubble growth model (Fig. 3) is adapted from the formulation of Proussevitch et al. [22]. At each new time step, $i+1$, a new magma pressure, $p_m^{i+1}=p_m^i- dp / dt$, is prescribed (see Table 1 for the symbols and notations used in this paper). This is equivalent to a constant mass flux, Q, at constant

Table 1
Symbols and notation

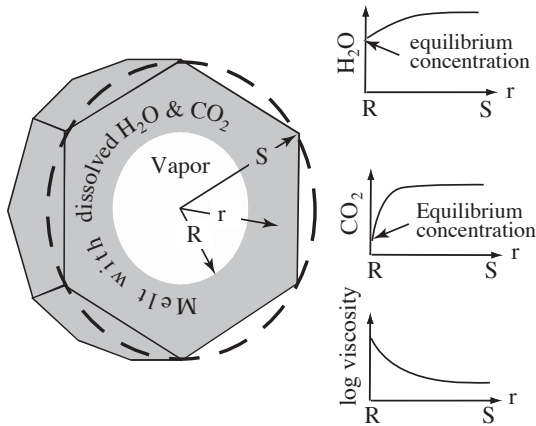| Symbol	Description	Value, units, ref.
0	Subscript denoting initial condition	
c_c	Concentration of CO_2 in melt	ppm
c_e	Equilibrium CO_2 concentration	ppm
c_m	CO_2 of Mono Craters sample	ppm
c_w	Concentration of H_2O in melt	wt.%
i	Index	
k	Magma permeability	m^2
m_g	Mass of exsolved gas	kg
p_g	Pressure of gas inside bubble	Pa
p_m	Pressure of the magma	Pa
dp / dt	Decompression rate	Pa s^{-1}
dp^* / dt^*	Nondimensional decompression rate	
$\dot{q}_v$	Volumetric gas flux	m s^{-1}
r	Radial distance from bubble center	m
t	Time	s
v_r	Radial velocity of melt	m s^{-1}
A	Cross-sectional area of conduit	m^2
C	Constant	0.2
D_c	Diffusivity of CO_2 in silicic melt	m^2 s^{-1}, [29–31]
D_w	Diffusivity of H_2O in silicic melt	m^2 s^{-1}, [38]
N	Number of Mono Craters samples	24
N_d	Bubble number density	m^{-3}
Q	Mass flux of magma	kg s^{-1}
R	Bubble radius	m
S	Radius of melt shell	m
T	Temperature	1123 K
X	Mole fraction of total H_2O, single oxygen basis	
α	Scaling parameter, open-system gas loss	
β	Weighting factor	
ϕ	Magma vesicularity	
ρ_g	Density of vapor phase	kg m^{-3} [37]
ρ_m	Melt density	2500 kg m^{-3}
μ_r	Melt viscosity	Pa s, [33]
μ_e	Effective melt viscosity	Pa s, [35]
μ_g	Viscosity of H_2O at 900	Pa s
σ	Surface tension	N m^{-1}, [36]
τ_D^{-1}	Characteristic diffusion rate	s^{-1}
τ_s^{-1}	Rate at which solubility changes	s^{-1}

Fig. 3. Schematic diagram of the diffusive bubble-growth model. Bubbles are assumed to coexist in a uniform polyhedral packing geometry, so that they can be represented by a spherical approximation (adopted from [22]). At the vapor–melt interface, vapor (CO_2+H_2O) coexists in equilibrium with dissolved CO_2 and H_2O, which diffuse radially down a concentration gradient to the melt–vapor interface where they exsolve. Because of surface tension the pressure of the gas inside the bubble is greater than the melt pressure, p_m. Exsolution and decreasing pressure cause the molar volume of the gas mixture to increase, resulting in bubble growth. Melt viscosity strongly depends on H_2O content [33] and increases radially across the melt shell as a consequence of volatile exsolution during decompression.

conduit cross-sectional area, A, and neglects dynamic pressure loss. Calculated pressure and velocity profiles (Fig. 4) are similar to those obtained from other conduit flow models at depths below the fragmentation depth (e.g., [23–25]). We do not explicitly model the coupled gas flow within the permeable magma, instead we evaluate open-system gas loss from a model for magma permeability (Section 2.6).
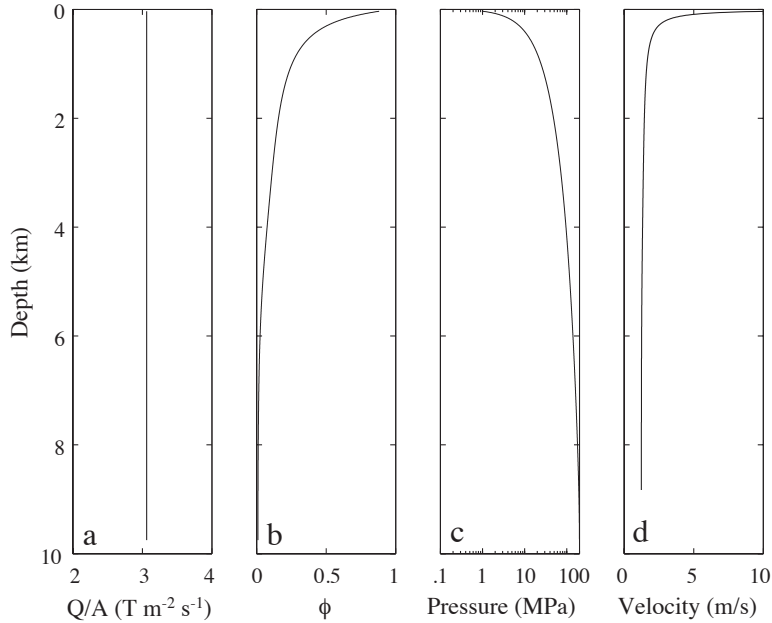
Fig. 4. Results from a typical model simulation with low degree of open-system gas loss. (a) Mass flow rate per unit area is constant. (b) Magma vesicularity increases as the magma ascends. The increase in vesicularity is most pronounced at shallow depths, where most of the H_2O exsolves. (c) Change in pressure as the magma ascends. Although we do not include dynamic pressure loss in our calculations, these results are similar to results from other conduit models (e.g., [23–25]), below the fragmentation depth. (d) Magma velocity as a function of depth. The magma accelerates during ascent, because of the increase in vesicularity at a constant mass flow rate.

2.1. H_2O and CO_2 solubility

The solubility of CO_2 and H_2O in silicate melts (Fig. 2), depend on temperature, pressure, and the composition of the already exsolved vapor phase (e.g., [26–28]). During equilibrium the concentration of each dissolved volatile species will be uniform throughout the melt and will be exactly equal to the equilibrium value for a given vapor composition. In a real magma, complete equilibrium may not be reached during ascent to the surface. However, the dissolved volatile concentration at the melt–vapor interface should always be in equilibrium with the exsolved vapor inside the bubble. Before reaching the melt–vapor interface and entering the bubble as vapor, volatiles have to diffuse through the surrounding melt shell (Fig. 3). The rate of diffusion is governed by the concentration gradient and the species-dependent diffusivity. The latter may depend on temperature, pressure, and composition [29–32]. Because solubilities decrease with pressure (Fig. 2), the concentration of CO_2 and H_2O at the vapor–melt interface will continuously decrease during magma

ascent. This sustains a concentration gradient across the melt shell, which depends on the relative decompression and diffusion rates. If decompression is sufficiently slow, relative to diffusion, the gradient will be small. If not, the average volatile concentration in the melt may be considerably larger than the equilibrium value (Fig. 3).

2.2. Bubble mass and momentum balance

At each p_m^{i+1}, new values of bubble radius, R^{i+1}, gas pressure inside the bubble, p_g^{i+1}, gas composition, as well as radially varying CO_2 and H_2O concentrations across the melt shell are calculated simultaneously. We denote the supercritical exsolved volatile phase within the bubble interchangeably as "gas" or "vapor". We assume isothermal conditions ($T = 900 \,^\circ C$) and include the effect of volatile dependent viscosity [33,34] through the use of an effective viscosity of the melt shell [35],

$$\mu_e = 3R^3 \int_R^S \frac{\mu(r, c_w)}{r^4} \, dr. \tag{1}$$

Here $S = (S_0^3 - R_0^3 + R^3)^{1/3}$ is the radius of the melt shell. The variables S_0 and R_0 are initial radii of the melt shell and bubble, respectively. μ_r is the radially varying viscosity of the melt, c_w is the weight fraction of H_2O dissolved in the melt, and r is radial distance from the center of the bubble (Fig. 3). Bubble growth requires the solution of the equation for momentum balance at the vapor–melt interface

$$p_g - p_m = \frac{2\sigma}{R} + 4\mu_e v_R \left(\frac{1}{R} - \frac{R^2}{S^3} \right). \tag{2}$$

Here p_g is the pressure of the vapor inside the bubble, p_m is the pressure of the melt surrounding the bubble, $v_R = dR/dt$ is the radial velocity of the bubble wall, and t denotes time. We use a surface tension for rhyolite, given by $\sigma = 0.11 + 0.013(0.052 - c_w)$ N m^{-1} [36]. The momentum equation is solved simultaneously with the equation for mass balance,

$$\frac{4\pi}{3} \frac{d}{dt} \left(R^3 \rho_g \right)$$
$$= 4\pi R^2 \rho_m \left[D_c \left(\frac{\partial c_c}{\partial r} \right)_{r=R} + D_w \left(\frac{\partial c_w}{\partial r} \right)_{r=R} \right]$$
$$+ \frac{\partial m_g}{\partial t}, \tag{3}$$

through an iterative scheme until convergence of all values is achieved. Here ρ_g is the pressure- and composition-dependent vapor density [37] and c_c is the weight fraction of dissolved CO_2.

2.3. Volatile diffusivities

The terms D_c and D_w in Eq. (3) are the diffusivity of CO_2 and of H_2O, respectively. A recent formulation for D_w is given by Zhang and Behrens [32]

$$D_w = 10^{-12}\exp[(14.08 - 13128/T - 2.796 p_m/T)$$
$$+ (-27.21 + 36892/T + 57.23 p_m/T)X]$$
$$\times 6.2 \times 10^{-7}\exp[-144600/(8.314\,T)], \tag{4}$$

where

$$X = \frac{c_w/0.1805}{c_w/0.18015 + (1 - c_w)/0.3249} \tag{5}$$

is the mole fraction of total H_2O dissolved in the melt on a single oxygen basis and T is in Kelvin.

The term D_w depends mostly on the concentration of dissolved H_2O and less on temperature and pressure. Under a broad range of conditions (dissolved H_2O concentration, pressure, and temperature) diffusion experiments indicate that D_c is typically about one order of magnitude smaller than D_w (e.g., [21,29–31]). Furthermore, it has been shown that D_c in silicate melts is essentially identical to the diffusivity of Argon [38,39]. In our model we therefore represent D_c by the formulation of Behrens and Zhang [38] for Argon

$$D_c = 10^{-12}\exp[(14.627 - 17913/T - 2.569 p_m/T)$$
$$+ (35936/T + 27.42 p_m/T)X] \times 6.2 \times 10^{-7}$$
$$\times \exp[-144600/(8.314\,T)]. \tag{6}$$

These diffusivity formulations give $D_c \approx D_w/3$ at $c_w = 0.05$ and $D_c \approx D_w/20$ at $c_w = 0.01$, with negligible pressure dependence between 0.1 MPa and 200 MPa. Until a consistent set of empirical D_c values for rhyolite at pressures of 200 MPa or less, and water contents of $0 \leq c_w \leq 0.05$ are available, we consider Eq. (6) most reliable for the range of water contents considered here. Larger estimates of D_c will not change our conclusions in essence, but will require higher decompression rates for nonequilibrium degassing to occur (see Section 2.7 for details).

2.4. Exsolution of volatiles from the melt

The left-hand side of the mass balance (Eq. (3)) describes the change in vapor mass inside the bubble and implicitly includes the bubble growth rate, dR/dt. The first term on the right-hand side represents the mass flux of CO_2 and H_2O into the bubble by exsolution. Mass flux by exsolution depends on the concentration gradient at the bubble interface, which is obtained by simultaneous solution of the diffusion equation for CO_2 and H_2O through the melt shell,

$$\frac{\partial c_s}{\partial t} + v_r \frac{\partial c_s}{\partial r} = \frac{1}{r^2} \frac{\partial}{\partial r} \left(D_s r^2 \frac{\partial c_s}{\partial r} \right). \tag{7}$$

Here the subscript s denotes either c for CO_2 or w for H_2O, and v_r is the radial velocity of the melt. Eq.

(7) is solved implicitly in a Lagrangian frame of reference and on a nonuniform grid to resolve steep concentration gradients near the vapor–melt interface [22]. The concentration at the bubble wall is the boundary condition for this equation and is given by the equilibrium solubility value at the given pressure, p_m^{i+1}, temperature ($T = 900$ °C), and mole fraction of CO_2 in the CO_2–H_2O vapor mixture inside the bubble. Because CO_2 and H_2O exsolve at different rates, the composition of the CO_2–H_2O vapor mixture changes with time. Here we use the recent empirical solubility model of Liu et al. [28]. We compared our model results to those obtained with the use of another solubility model [27] and find that our model results are almost identical.

2.5. Open-system gas loss

The last term of the equation of mass balance (3), $\partial m_g / \partial t$, denotes the rate of mass loss by open-system degassing. We consider the two cases:

$$\frac{\partial m_g}{\partial t} = 0 \text{ (closed system)} \tag{8}$$

and

$$\frac{\partial m_g}{\partial t} = \alpha \frac{\pi S^2 \rho_g k}{\mu_g} \nabla p_g \text{ (open system)}. \tag{9}$$

Here μ_g is the viscosity of H_2O at 900 °C and given pressure, and ∇p_g represents the characteristic pressure gradient that drives permeable gas flow through the magma. In our model k is determined through an empirical scaling relation (see Section 2.6). Eq. (9) is derived from Darcy's law, which states that $\dot{q}_v / (\pi S^2)$, the volumetric flow rate per cross-sectional area (in our case of an individual bubble), is proportional to the product of permeability, k, and gas pressure gradient, ∇p_g. We neglect inertial effects associated with open-system gas flow [40] and assume instantaneous mixing of exsolved vapor prior to open-system gas loss. The change in gas density throughout magma ascent is taken into account through the modified Redlich–Kwong Equation of State [37].

We assume that ∇p_g is constant throughout magma ascent at 10^5 Pa m^{-1}, which represents a conservatively low value [3]. Gas loss from the magma should be proportional to the gas flux through the permeable magma. Because we do not explicitly model gas flow through the magma, we use the scaling parameter α to account for the fact that the rate of open-system gas loss from individual bubbles is only a small fraction of the total gas flux. Vesicularity and open-system gas loss do not vary radially in our model which is motivated by the prevalent view that open-system degassing occurs via permeable gas flow through the porous magma (e.g., [2,3,5,7]). Our choice of α will be discussed in Section 3.4.2.

2.6. Magma permeability

Magma permeability is thought to be proportional to magma porosity, ϕ (e.g., [2,40–45]). We assume that porosity and vesicularity are equal and use the permeability model (e.g., [42,44])

$$k \propto \phi R^2. \tag{10}$$

We have found that similar model results can be achieved using other formulations (e.g., [2,41,45]).

2.7. Bubble number density

Bubble number density, N_d, of silicic magmas varies over several orders of magnitude (e.g., [44,46]) and is generally thought to be a function of volatile supersaturation and bubble nucleation rate (e.g., [47–50]), as well as bubble coalescence (e.g., [51]). Accordingly, we vary N_d over a broad range in our model simulations. The rate of volatile exsolution, τ_D^{-1}, is a function of volatile diffusivity, D, and is inversely dependent on the square of the melt thickness around individual bubbles, $\tau_D^{-1} \propto D/(S-R)^2$. Substituting the relations $N_d = 3/4\pi S^3$ and $\phi = (R/S)^3$ results in the scaling

$$\tau_D^{-1} \propto D N_d^{2/3} \left(1 - \phi^{1/3}\right)^{-2}. \tag{11}$$

The volatile concentration at the melt–vapor interface is a function of magma pressure. Hence, the rate at which volatile concentration at the melt–vapor interface decreases is a function of decompression rate, $p_0/\tau_s \propto \mathrm{d}p/\mathrm{d}t$. During diffusive bubble growth equilibrium can be maintained if $\tau_s^{-1} \leq \tau_D^{-1}$. In other

words, the transition to nonequilibrium during decompression should follow the scaling

$$\frac{dp}{dt} \propto p_{m,0} D N_d^{2/3} \left(1 - \phi^{1/3}\right)^{-2}. \tag{12}$$

In model simulations with significant open-system gas loss ($\phi \lesssim 0.01$), the term $(1 - \phi^{1/3})^{-2}$ is approximately constant and $dp/dt \propto N_d^{2/3}$. We find that this scaling also holds if open-system gas loss is smaller.

3. Model results

We compare model results from nonequilibrium degassing simulations with results from equilibrium degassing models at the same conditions. We examine a range of parameters, of which the decompression (ascent) rate and bubble number density are of primary importance. All model simulations start at an initial pressure of $p_{m,0}=200$ MPa. Initial volatile concentrations are equilibrium solubility values at 200 MPa and represent a reasonable choice for comparison with the Mono Craters data (e.g., [9]), as well as many other silicic eruptions (e.g., [13]).

3.1. Mono Craters CO_2–H_2O degassing trend

CO_2 and H_2O concentrations of Mono Craters pyroclastic obsidian samples delineate an apparent degassing trajectory (Fig. 5). However, Mono Cra-
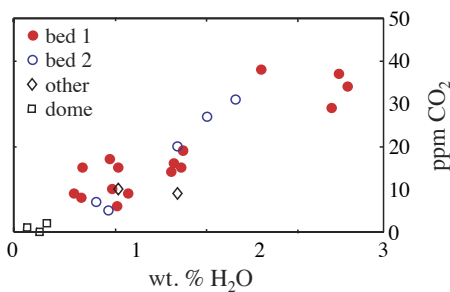

Fig. 5. CO_2 versus H_2O concentrations of Mono Craters pyroclastic obsidian samples [9]. Mono Craters tephras are well-bedded [52,53] and have been interpreted to be the result of a pulsatory subplinian eruption [54]. Most measured concentrations are from beds 1 (dots) and 2 (open circles). Concentrations from beds other than 1 and 2 are shown undifferentiated as open diamonds. Dome samples are shown as open squares.

ters tephras are well-bedded [52,53] and have been interpreted as the result of a pulsatory subplinian eruption [54]. Concentration values within individual beds may be interpreted to represent different "quench" or "fragmentation" depths associated with somewhat varying ascent rates. From our analysis we find that the overall variability in eruption parameters, capable of reproducing Mono Craters concentration values, is relatively small Therefore, we present model results in terms of a best-fit to all pyroclastic Mono Crater samples. However, the reader should easily be able to extrapolate to individual samples, or sample groupings.

3.2. Closed-system degassing

During closed-system degassing all volatiles that exsolve from the melt remain as vapor within the bubbles. Fig. 6 shows the results from an equilibrium closed-system (long-dashed), a CO_2-rich equilibrium closed-system (short-dashed), and a nonequilibrium closed-system (solid) degassing model. These examples are discussed next.

3.2.1. Equilibrium
The equilibrium closed-system model is our reference model (Fig. 6, long dashed). It assumes that the initial volatile concentrations in melt and vapor phases are in equilibrium at an initial pressure of $p_m=200$ MPa. Initial values are $\phi_0=1\%$, $c_{w,0}=4.6$ wt.%, $c_{c,0}=354$ ppm, and an initial CO_2 mole fraction in the gas phase of 0.29. At 1% vesicularity, the total mass of CO_2 in the system is equivalent to approximately 700 ppm. Because of the low solubility of CO_2 relative to H_2O, decompression results in a degassing trend with lower CO_2 concentrations than Mono Craters samples (Fig. 6f,). For the equilibrium model, H_2O and CO_2 concentrations are constant throughout the melt and decrease during ascent (Fig. 6c,d), while vesicularity increases as H_2O and CO_2 exsolve (Fig. 6e).

3.2.2. CO_2-rich equilibrium
A better fit to the Mono Craters data is obtained by a model with an initial vesicularity of 20% (Fig. 6, short dashed), but otherwise identical initial conditions. This model is also limited in its ability to fit CO_2 concentrations at <1 wt.% H_2O. It is equiva-
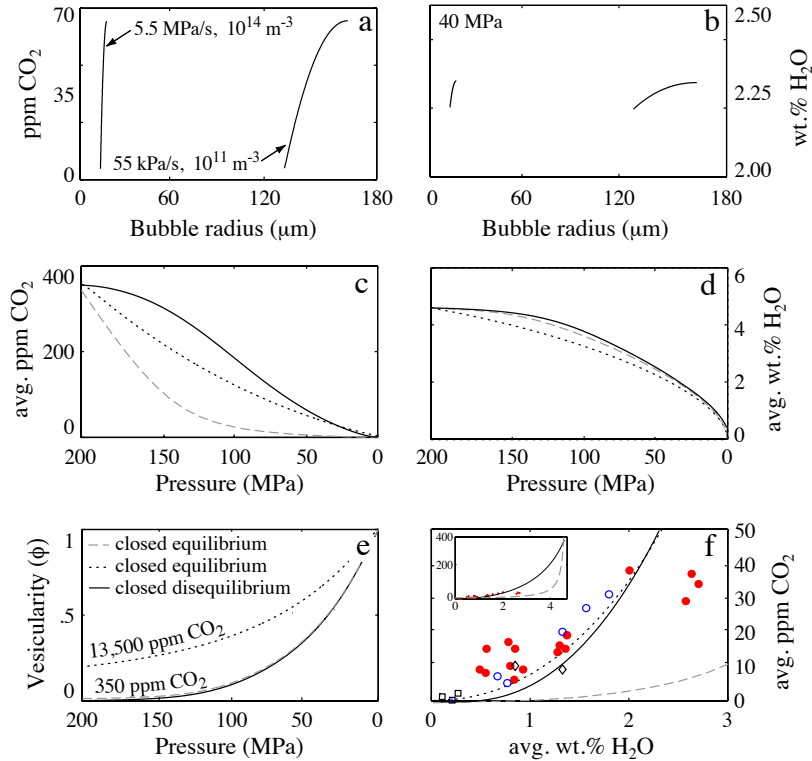
Fig. 6. *Long dashed*: Model results for equilibrium, closed-system degassing. Initial conditions are $p_{m,0}=200$ MPa, $\phi_0=1\%$, $c_{w,0}=4.6$ wt.%, and $c_{c,0}=387$ ppm. Initial values of H_2O and CO_2 correspond to a mole fraction of CO_2 for the vapor phase of 0.29. Volatile concentrations in the melt are constant and concentration profiles for this case are not shown. *Short dashed*: Equilibrium, closed-system case with identical initial conditions, except $\phi_0=20\%$. This case is similar to the model by Newman et al. [9] and requires a pre-eruptive CO_2 content of the magma of approximately 1.39 wt.%. *Solid*: Nonequilibrium, closed-system with identical initial conditions to the equilibrium, closed-system case with $\phi_0=1\%$ (long-dashed). (a) and (b) are concentration profiles for two different model simulations, one with $dp/dt=5.5\times10^4$ Pa s^{-1} and $N_{d,0}=10^{11}$ m^{-3}, and the second with $dp/dt=5.5\times10^6$ Pa s^{-1} and $N_{d,0}=10^{14}$ m^{-3}. Because of the tradeoff between dp/dt and N_d, the two cases are essentially identical (c–f). Because CO_2 degassing is not in equilibrium, these models provide a very similar fit to Mono Craters concentrations as the equilibrium case with $\phi_0=20\%$. (f) Inset shows the complete degassing trend.

lent to the model of Newman et al. [9] and requires a total abundance of approximately 13,900 ppm CO_2, most of which is already exsolved at $p_m=200$ MPa. Because H_2O concentrations in the melt are about a factor of 100 larger than CO_2 concentrations, decompression results in a continuous decrease in the mole fraction of exsolved CO_2, despite the higher solubility of H_2O. The large initial abundance of exsolved CO_2 is required to maintain a relatively high CO_2 mole fraction of the vapor phase throughout magma ascent, which in turn leads to increased equilibrium CO_2 solubilities (Fig. 2). The required CO_2 content for this model implies a high CO_2 abundance in the parental

magma, with CO_2 saturation at pressures of approximately 1400 MPa.

3.2.3. Nonequilibrium

Fig. 6 (solid) shows the results of two closed-system nonequilibrium model calculations with degassing trajectories similar to the closed-system, CO_2-rich case (Fig. 6f). One of these models is for $dp/dt=5.5$ MPa s^{-1} and $N_d=10^{14}$ m^{-3}, while the second case is for $dp/dt=0.055$ MPa s^{-1} and $N_d=10^{11}$ m^{-3}. The model results for both cases differ only in their concentration profiles (Fig. 6a,b). This invariance is a consequence of the tradeoff between dp/dt and N_d (Eq. (12)). The volume-

trically averaged CO_2 concentrations of the melt (Fig. 6c) are considerably higher than equilibrium values. This is a consequence of slow CO_2 diffusion relative to the decrease in solubility values at the melt–vapor interface. Because D_w is sufficiently large, H_2O concentrations barely depart from equilibrium (Fig. 6d). A large initial volume of exsolved CO_2 is not required and vesicularities are similar to those from the closed-system equilibrium case (Fig. 6e).

3.2.4. Sensitivity to decompression rate

Fig. 7 shows the sensitivity of the nonequilibrium model to decompression rate, dp/dt. A decrease in dp/dt will shift estimated CO_2/H_2O values toward equilibrium and no longer provides a good match to Mono Craters concentrations. An increase in dp/dt will steepen the degassing trend so that CO_2 con-

centrations at <1 wt.% H_2O match Mono Craters values, while CO_2 concentrations at higher H_2O are significantly overestimated.

All concentrations from Bed 2 are well matched by a single degassing trajectory with $dp/dt \approx 70$ kPa s^{-1} and quench depths of less than 30 MPa (Fig. 7f). If dp/dt is varied by a factor of approximately 2, all other concentration values can be fit as well and have quench depths of less than 60 MPa. However, closed-system models alone cannot explain the formation of obsidian, as they will result in highly vesicular magma (Fig. 7e).

3.3. Open-system

Our open-system models are motivated by the objective of finding a degassing trend that (1) provides
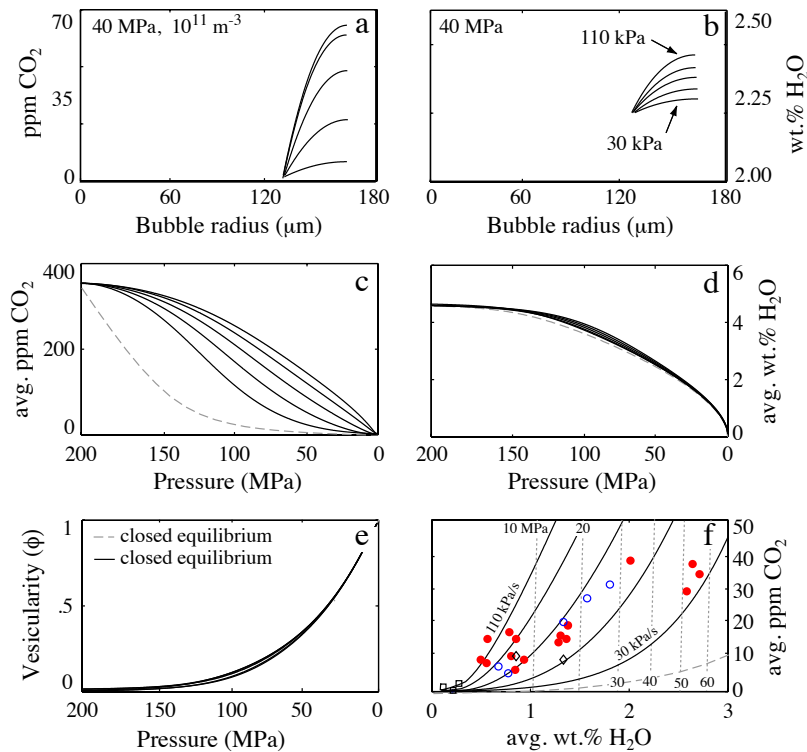

Fig. 7. Model results for closed-system degassing with different dp/dt. For reference, the long-dashed curves are the equilibrium, closed-system case. Initial conditions are $p_{m,0}=200$ MPa, $\phi_0=1\%$, $N_{d,0}=10^{11}$ m^{-3}, $c_{w,0}=4.6$ wt.%, and $c_{c,0}=387$ ppm. Initial values of H_2O and CO_2 correspond to a mole fraction of CO_2 for the vapor phase of 0.29. Decompression rates range between $dp/dt=5\times10^4$ Pa s^{-1} and $dp/dt=11\times10^4$ Pa s^{-1} in increments of 2×10^4 Pa s^{-1}. CO_2 concentration profiles (a) indicate that disequilibrium degassing of CO_2 increases with increasing decompression rate. This is also evident from the average CO_2 concentrations of the melt (c) and the degassing trends (f). H_2O degassing barely departs from equilibrium (a, d). Because these models represent closed-system degassing, vesicularities are almost identical to the equilibrium, closed-system case (e). In (f), vertical dashed lines with labels indicate p_m.

a reasonable match to the Mono Craters CO_2–H_2O concentrations, and (2) results in a magma vesicularity that is consistent with obsidian formation. For a given value of N_d we first find the smallest value of α that meets the constraint $\phi \leq 0.01$ at $p_m \geq 2.5$ MPa (lithostatic pressure at approximately 100 m depth). We then determine the corresponding value of dp/dt that results in a best fit to the Mono Craters data for the given values of N_d and α. Several open-system model simulations are discussed subsequently.

3.3.1. Open

Fig. 8 (solid) shows the result of a nonequilibrium open-system degassing model with a good fit to the Mono Craters data with $\phi \leq 0.01$. Similar to closed-system models, small variations in ascent conditions ($dp/dt < \pm 10\%$) will shift the simulated degassing trend sufficiently to match individual samples. Fig. 8 (solid) shows two cases, $N_d = 10^{11}$ m^{-3} with $dp/dt = 3.22$ kPa s^{-1}, and $N_d = 10^{14}$ m^{-3} with $dp/dt = 322$ kPa s^{-3}. Except for concentration profiles (Fig. 8a,b), the degassing trends of these two cases are virtually indistinguishable, because of the tradeoff between dp/dt and N_d. Concentrations of CO_2 within the melt shell range from almost 0 ppm to approximately 30 ppm (Fig. 8a). That average CO_2 concentrations (Fig. 8c) are noticeably higher than equilibrium concentrations (long dashed). H_2O concentrations on
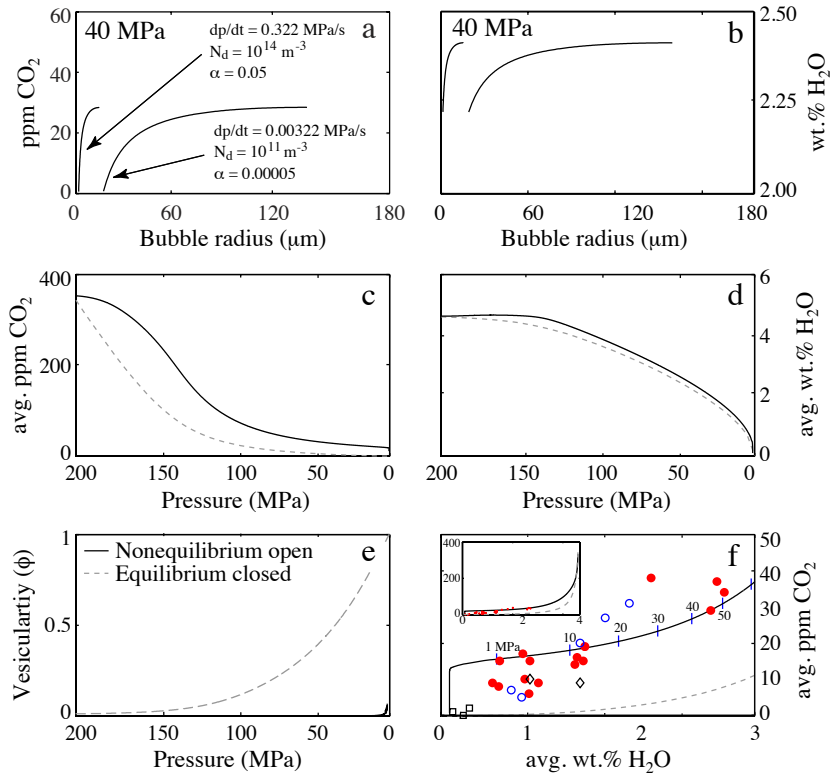

Fig. 8. Model results for open-system degassing. Initial conditions are $p_{m,0} = 200$ MPa, $\phi_0 = 1\%$, $c_{w,0} = 4.6$ wt.%, and $c_{c,0} = 387$ ppm. Initial values of H_2O and CO_2 correspond to a mole fraction of CO_2 for the vapor phase of 0.29. The closed-equilibrium reference case is shown as the long-dashed curves. Two cases are shown: $dp/dt = 3.22 \times 10^3$ Pa s^{-1} with $N_{d,0} = 10^{11}$ m^{-3}, and $dp/dt = 3.22 \times 10^5$ Pa s^{-1} with $N_{d,0} = 10^{14}$ m^{-3}. Because of the tradeoff between N_d and dp/dt, model results (other than concentration profiles) are essentially indistinguishable for the two cases. CO_2 concentrations are in disequilibrium (a, c), whereas H_2O concentrations are close to equilibrium (b, d). Because of open-system gas loss, ϕ remains small (~1%) throughout magma ascent. The steep decrease in CO_2 at the end of the degassing trajectory occurs during prolonged repose at atmospheric pressure. Open-system degassing predominantly inhibits CO_2 exsolution at relatively shallow depths, relative to the closed-system case shown in Fig. 7. In (f), short vertical lines with numbers denote pressure, p_m, in MPa and inset shows the complete degassing trend.

the other hand are close to equilibrium throughout magma ascent and concentration gradients across the melt shell are small (Fig. 8b, d). High CO_2 concentrations are solely the consequence of CO_2 diffusion rates that are slower than the rate at which solubility decreases, as opposed to buffering by a CO_2-rich vapor phase ([9,10]).

3.3.2. Slightly open

Fig. 9 (solid) shows the result of a nonequilibrium open-system degassing scenario with a good fit to the Mono Craters data. In this case open-system gas loss is not sufficient to maintain a low vesicularity (small α). Two cases are shown: $N_d = 10^{11}$ m^{-3} with $dp/dt = 19$ kPa s^{-1}, and $N_d = 10^{14}$ m^{-3} with $dp/dt = 1.9$ MPa s^{-1}. Because of the tradeoff between dp/dt and N_d, only the concentration profiles are noticeably different between these two cases (Fig. 9a,b). Overall, results

for this model fall between the fully open-system case (Fig. 8) and the nonequilibrium closed-system cases (Fig. 7). Open-system gas loss results in higher CO_2 concentrations, most notably at low H_2O values. The model provides a good fit to Mono Craters data, but produces a magma with considerable vesicularity.

3.3.3. Open at ≤25 MPa

Fig. 9 (short dashed) shows the result of a nonequilibrium degassing scenario with a transition from closed- to open-system degassing at a pressure of 25 MPa, with $dp/dt = 4.5$ MPa s^{-1} and $N_d = 10^{14}$ m^{-3}. This case is representative of ascent conditions where open-system gas loss is only significant at relatively shallow depths. This might, for example, be the case if open-system gas loss is predominantly into conduit walls with low permeabilities at greater depths. This case also provides a reasonable match to Mono Cra-
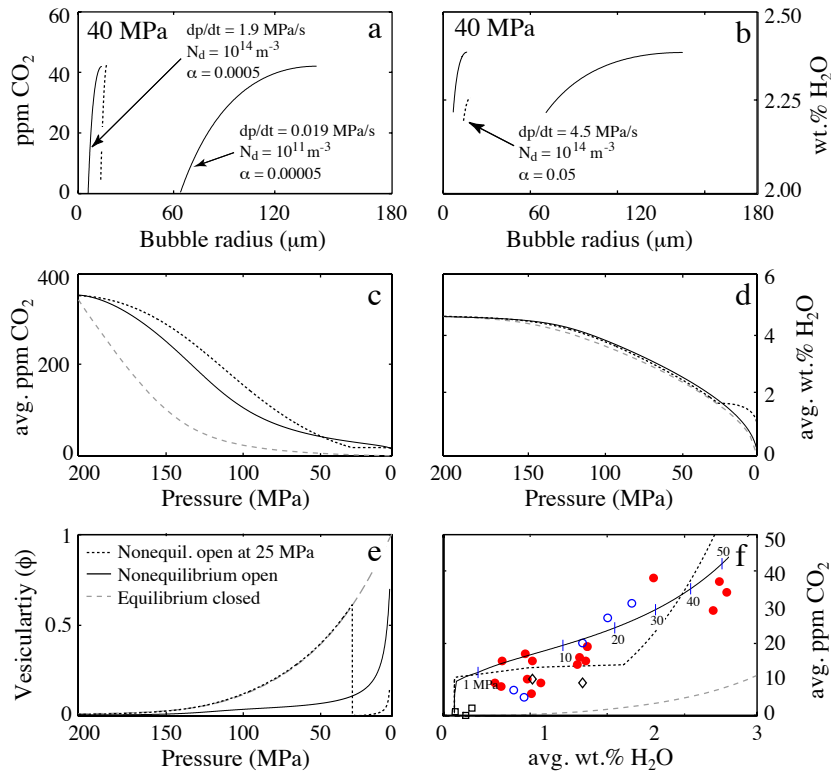

Fig. 9. Model results for limited open-system degassing. *Solid*: Low degree of open-system degassing throughout magma ascent. Identical to (Fig. 8), but with a smaller value of α and a 6-fold increase in dp/dt. *Short dashed*: Nonequilibrium closed-system degassing with a transition to open-system degassing at $p_m \leq 25$ MPa with $dp/dt = 4.5 \times 10^6$ Pa s^{-1} and $N_{d,0} = 10^{14}$ m^{-3} (short dashed), but otherwise identical to the model shown in (Fig. 8). As in the model of (Fig. 8), open-system degassing predominantly inhibits CO_2 exsolution at relatively shallow depths, relative to the closed-system case. In (f), short vertical lines with numbers denote pressure, p_m, in MPa.
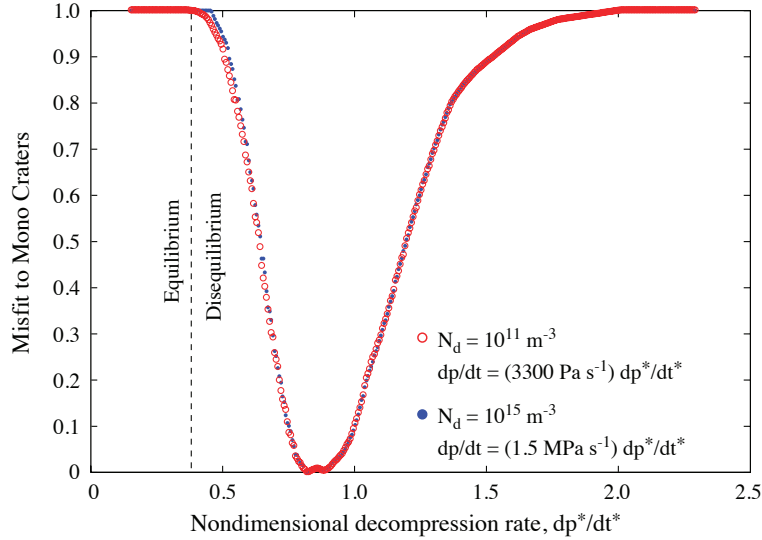
Fig. 10. Results from a sensitivity analysis for dp/dt and N_d. Each data point represents model misfit to Mono Craters CO_2 concentrations from one model simulation. Solid dots are for $N_d=10^{15}$ m^{-3} and open circles are for $N_d=10^{11}$ m^{-3}. The superposition of the two curves is a consequence of the tradeoff between N_d and dp/dt. The transition from equilibrium to nonequilibrium degassing occurs at $dp*/dt*$ 0.4($dp/dt* \approx 1.3 \times 10^4$ Pa s^{-1} for $N_d=10^{11}$ m^{-3} and $dp/dt \approx 6 \times 10^6$ Pa s^{-1} for $N_d=10^{15}$ m^{-3}). The best fit to Mono Craters data is at $dp*/dt* \approx 0.8$.

ters data, but requires an approximately 10-fold increase in decompression rate.

3.4. Model sensitivity analysis

In this Section we provide an analysis of model sensitivity to α, dp/dt, and N_d.

3.4.1. Best fit

We evaluate our model results in terms of a best fit to Mono Craters CO_2 vs. H_2O concentrations. We define the best fit to Mono Craters data as

$$\sum_{i=1}^{N} \left(\beta_i \min\left[1, \frac{|c_{m,i} - c_{c,i}|}{c_{m,i} - c_{e,i}} \right] \right) \left(\sum_{i=1}^{N} \beta_i \right)^{-1}, \qquad (13)$$

where index i is from lowest to highest H_2O concentration of Mono Craters pyroclastic obsidian samples, $c_{m,i}$ is the CO_2 concentration of the ith sample, $c_{e,i}$ is the CO_2 concentration of the equilibrium, closed-system degassing model (Fig. 6, long-dashed) at the same dissolved H_2O concentration as the corresponding Mono Craters sample, and $c_{c,i}$ is the corresponding CO_2 concentration of the given model simulation. The factor β_i scales the ith CO_2

misfit value so that there is no artificial bias toward sample clusters at various H_2O concentrations. Accordingly, β_i is defined as

$$\beta_i = 2\left(c_{w,i+1} - c_{w,i} \right) \qquad i = 1,$$

$$\beta_i = \left(c_{w,i+1} - c_{w,i-1} \right) \qquad 1 < i < N,$$

$$\beta_i = 2\left(c_{w,i} - c_{w,i-1} \right) \quad i = N. \qquad (14)$$

3.4.2. Model sensitivity to α

For high degrees of open-system gas loss (Fig. 8) at different values of N_d, we find that the scaling $N_d/\alpha = 2 \times 10^{-3}$ µm^{-3} has to apply to achieve an equivalent degree of outgassing. For cases where open-system gas loss is less pronounced (Fig. 9), this sensitivity no longer holds.

3.4.3. Model sensitivity to dp/dt and N_d

Almost identical model results are achieved if $dp/dt \propto N_d^{2/3}$. Accordingly, we define a nondimensional decompression rate

$$\frac{dp*}{dt*} = \frac{dp}{dt} \left(p_{m,0} D_{c,0} N_d^{2/3} \right)^{-1}, \qquad (15)$$

where $p_{m,0}=200$ MPa and $D_{c,0}=7.6\times10^{-13}$ m^2 s^{-1}. In Fig. 10 we show the misfit of model results to Mono Craters data as a function of $dp*/dt*$. Each symbol represents an individual model simulation where open circles are for $N_d=10^{11}$ m^{-3}, and solid dots are for $N_d=10^{14}$ m^{-3}. Model results are almost identical for the two different values of N_d, provided that $dp/dt \propto N_d^{2/3}$.

The fit to Mono Craters data is relatively sensitive to changes in N_d or $dp*/dt*$ (Fig. 10). Decreasing dp/dt by a factor of 0.5, or increasing N_d by a factor of 2.5, will change open-system model results from a nonequilibrium best fit to equilibrium values. Although our analysis is cast in terms of a best fit to Mono Craters data, the transition from equilibrium to disequilibrium is equally applicable to other cases. The same is true for the tradeoff between N_d and dp/dt.

4. Discussion

4.1. Degassing of Mono Craters pyroclastic obsidian samples

Based on volumetric eruption-rate estimates by Bursik [54], decompression rates for Mono Craters magma can be estimated as $dp/dt \sim 10^3$ Pa s^{-3} (0.1 m s^{-1}). Nonequilibriuim therefore requires that average bubble number density during magma ascent is $\leq10^{11}$ m^{-3}. This is feasible, because most bubble nucleation may occur at relatively shallow levels (e.g., [25,49,50]). Moreover, Mono Craters dome pumice, generally found in contiguous samples of obsidian bound by pumice, has $N_d \leq 10^{11}$ m^{-3} ($\phi \leq 0.7$ and $R \leq 100$ μm) [55,56]. If Mono Craters pyroclastic pumice is associated with a shallow nucleation event [49] and the ascending magma had low bubble number densities during most of its ascent (similar to those found in dome pumice) then CO_2/H_2O concentration ratios of Mono Craters pyroclastic obsidian may indeed record nonequilibrium magma degassing. If this is the case, then CO_2/H_2O concentrations provide a relatively sensitive constraint on magma ascent conditions.

Tephra samples from Mono Craters (Panum Crater) have $N_d \sim 10^{13}$ m^{-3} ($R \sim 10$ μm and $\phi \sim 0.1$) [57]. If these bubble number densities are the consequence of early bubble nucleation at depth, then

$dp*/dt* \sim 0.01$, and observed CO_2 and H_2O concentrations cannot be the consequence of nonequilibrium degassing.

To summarize, open-system degassing during magma ascent is consistent with the formation of extensively degassed obsidian. Model simulations, that closely match the Mono Craters volatile concentrations, can retain low vesicularities (~1%) throughout magma ascent by open-system degassing. However, this requires low bubble nucleation rates and smaller bubble number densities than Mono Craters pyroclastic pumice [57] during most of the magma ascent. In the subsequent Sections we discuss two alternative scenarios and their implications for the formation of pyroclastic obsidian with Mono Craters volatile concentrations.

4.1.1. Stalled magma

It has been suggested that pyroclastic obsidian clasts represent magma that somehow stalled within the conduit, or welded onto the conduit walls [58], thereby allowing sufficient time for open-system degassing to low vesicularity. This is not a feasible hypothesis for Mono Craters pyroclastic obsidian, because dissolved CO_2 concentrations would quickly approach equilibrium values in the stalled magma.

4.1.2. Autobrecciation

An alternative conceptual model is that of magma autobrecciation along the conduit walls [10–12,59]. This process would release gas from bubbles by fracturing of bubble walls and simultaneously result in the formation of a highly permeable fracture network leading to rapid gas loss and obsidian formation. This has been proposed in several recent studies [10–12,59,60] and could be a consequence of intense shear-strain rates near the conduit walls [11,12,61].

If autobrecciation took place throughout magma ascent and resulted in a low bubble number density, then nonequilibrium degassing was feasible and would not require a CO_2-rich volatile flux [10]. However, autobrecciation may only occur at shallow depths, for example caused by rapid acceleration just below the fragmentation depth. In this case, a low bubble number density would be necessary to explain Mono Craters CO_2–H_2O concentrations by nonequilibrium degassing prior to autobrecciation.

If degassing prior to autobrecciation was in nonequilibrium and in a closed-system, then volatile concentrations of the ascending magma followed degassing trajectories like those shown in Fig. 7f. Once autobrecciation destroyed bubbles, further volatile exsolution may have been inhibited because of the absence of vesicles. For example, samples from Bed 2 (Fig. 7f, open circles) may simply record different autobrecciation depths. Regardless, the equilibrium degassing models proposed by Newman et al. [9] and by Rust et al. [10] remain viable alternatives.

5. Conclusions

Our model simulations indicate that volatile concentrations measured in pyroclastic obsidian from the ca. 1340 A.D. Mono Craters eruption [9] are well explained by nonequilibrium degassing of the ascending magma. The required initial CO_2 content of the magma is less than 0.1 wt.% and does not necessitate volatile oversaturation, or an exsolved vapor phase, prior to eruption. Permeability-controlled, open-system gas loss can explain obsidian formation and enhances nonequilibrium during degassing at shallow levels. If open-system gas loss, by permeable gas flow throughout magma ascent, is insufficient for obsidian formation, some process like autobrecciation may be required. In this case, Mono Craters CO_2–H_2O concentration could be the consequence of nonequilibrium degassing, or the presence of a CO_2-rich vapor phase [9,10]. Nonequilibrium degassing is only viable if bubble number densities are sufficiently low during magma ascent ($N_d \leq 10^{11}$ m^{-3} in the case of Mono Craters), which could be the case if bubble nucleation occurs predominantly at shallow depths. Magma with a low bubble number density has thick melt shells that surround bubbles. This can result in nonequilibrium, because the rate of CO_2 diffusion through the relatively thick melt can be slower than the rate at which CO_2 solubility decreases due to decompression.

Acknowledgments

References

[1] R.S.J. Sparks, The dynamics of bubble formation and growth in magmas: a review and analysis, J. Volcanol. Geotherm. Res. 3 (1978) 1–37.

[2] J.C. Eichelberger, C.R. Carrigan, H.R. Westrich, R.H. Price, Non-explosive silicic volcanism, Nature 323 (1986) 598–602.

[3] C. Jaupart, C.J. Allègre, Gas content, eruption rate and instabilities of eruption regime in silicic volcanoes, Earth Planet. Sci. Lett. 102 (1991) 413–429.

[4] A.W. Woods, T. Koyaguchi, Transitions between explosive and effusive eruption of silicic magmas, Nature 370 (1994) 631–645.

[5] C. Jaupart, Gas loss from magmas through conduit walls during eruption, in: J.S. Gilbert, R.S.J. Sparks (Eds.), The Physics of Explosive Volcanic Eruptions, vol. 145, Geological Society, London, 1998, pp. 73–90.

[6] J.C. Eichelberger, Silicic volcanism: ascent of viscous magmas from crustal reservoirs, Annu. Rev. Earth Planet. Sci. 23 (1995) 41–63.

[7] M.V. Stasiuk, J. Barclay, M.R. Carroll, C. Jaupart, J.C. Ratté, R.S.J. Sparks, S.R. Tait, Degassing during magma ascent in the Mule Creek vent (USA), Bull. Volcanol. 58 (1996) 117–130.

[8] B. Villemant, G. Boudon, Transition from dome-forming to Plinian eruptive styles controlled by H_2O and Cl degassing, Nature 392 (1998) 65–69.

[9] S. Newman, S. Epstein, E.M. Stolper, Water, carbon dioxide, and hydrogen isotopes in glasses from the ca. 1340 A.D. eruption of the Mono Craters, California: constraints on degassing phenomena and initial volatile content, J. Volcanol. Geotherm. Res. 35 (1988) 75–96.

[10] A.C. Rust, K.V. Cashman, P.J. Wallace, Magma degassing buffered by vapor flow through brecciated conduit margins, Geology 32 (2004) 349–352.

[11] H.M. Gonnermann, M. Manga, Explosive volcanism may not be an inevitable consequence of magma fragmentation, Nature 426 (2003) 432–435.

[12] H. Tuffen, D.B. Dingwell, H. Pinkerton, Repeated fracture and healing of silicic magma generate flow banding and earthquakes? Geology 31 (2003) 1089–1092.

[13] B. Scaillet, M. Pichavant, Experimental constraints on volatile abundances in arc magmas and their implications for degassing processes, Geol. Soc. Spec. Publ. 213 (2003) 23–52.

[14] T. Casadevall, W. Rose, T. Gerlach, L.P. Greenl, J. Ewert, R. Symonds, Gas emissions and the eruptions of Mount St. Helens through 1982, Science 221 (1983) 1383–1385.

[15] P.J. Wallace, A.T. Anderson Jr., A.M. Davis, Quantification of pre-eruptive exsolved gas contents in silicic magmas, Nature 377 (1995) 612–616.

[16] W. Hildreth, Volcanological perspectives on Long Valley, Mammoth Mountain, and Mono Craters: several contiguous but discrete systems, J. Volcanol. Geotherm. Res. 136 (2004) 169–198.

[17] P.J. Wallace, Volatiles in subduction zone magmas: concentrations and fluxes based on melt inclusion and volcanic gas data, J. Volcanol. Geotherm. Res. 140 (2005) 217–240.

[18] P. Papale, Determination of total H_2O and CO_2 budgets in evolving magmas from melt inclusion data, J. Geophys. Res. 110 (2005), doi:10.1029/2004JB003033.

[19] M. Manga, E. Brodsky, Seismic triggering of eruptions in the far field: volcanoes and geysers, Ann. Rev. Earth Planet. Sci. (in press).

[20] A. Namiki, M. Manga, Response of a bubble-bearing viscoelastic fluid to rapid decompression: implications for explosive volcanic eruptions, Earth Planet. Sci. Lett. 236 (2005) 269–284.

[21] E.B. Watson, Diffusion of dissolved CO_2 and Cl in hydrous silicic to intermediate magmas, Geochim. Cosmochim. Acta 55 (1991) 1897–1902.

[22] A. Proussevitch, D. Sahagian, A. Anderson, Dynamics of diffusive bubble growth in magmas: isothermal case, J. Geophys. Res. 98 (1993) 22,283–22,307.

[23] P. Papale, Strain-induced magma fragmentation in explosive eruptions, Nature 397 (1999) 425–428.

[24] L. Mastin, Insights into volcanic conduit flow from an open-source numerical model, Geochem. Geophys. Geosyst. 3 (2002), doi:10.1029/2001GC000192.

[25] M. Mangan, L. Mastin, T. Sisson, Gas evolution in eruptive conduits: combining insights from high temperature and pressure decompression experiments with steady-state flow modeling, J. Volcanol. Geotherm. Res. 129 (2004) 23–36.

[26] P. Papale, Modeling of the solubility of a two-component H_2O+CO_2 fluid in silicate liquids, Am. Mineral. 84 (1999) 477–492.

[27] S. Newman, J.B. Lowenstern, VOLATILECALC: a siliate melt–H_2O–CO_2 solution model written in Visual Basic for Excel, Comput. Geosci. 28 (2002) 597–604.

[28] Y. Liu, Y. Zhang, H. Behrens, Solubility of H_2O in rhyolitic melts at low pressures and a new empirical model for mixed H_2O–CO_2 solubility in rhyolitic melts, J. Volcanol. Geotherm. Res. 143 (2005) 219–235.

[29] J.G. Blank, E.M. Stolper, Y. Zhang, Diffusion of CO_2 in rhyolitic melt, Trans. Am. Geophys. Union 75 (1991) 353.

[30] J.G. Blank, An experimental investigation of the behavior of carbon dioxide in rhyolitic melt, Ph.D. thesis, California Institute of Technology (1993).

[31] E.B. Watson, Diffusion in volatile-bearing magmas, Rev. Miner. 30 (1994) 371–411.

[32] Y.X. Zhang, H. Behrens, H_2O diffusion in rhyolitic melts and glasses, Chem. Geol. 169 (2000) 243–262.

[33] K.U. Hess, D.B. Dingwell, Viscosities of hydrous leucogranitic melts: a non-Arrhenian model, Am. Mineral. 81 (9–10) (1996) 1297–1300.

[34] J.D. Blower, H.M. Mader, S.D.R. Wilson, Coupling of viscous and diffusive controls on bubble growth during explosive volcanic eruptions, Earth Planet. Sci. Lett. 193 (2001) 47–56.

[35] N. Lensky, V. Lyakhovsky, O. Navon, Radial variations of melt viscosity around growing bubbles and gas overpressure in vesiculating magmas, Earth Planet. Sci. Lett. 186 (2001) 1–6.

[36] M. Mangan, T. Sisson, Evolution of melt–vapor surface tension in silicic volcanic systems: experiments with hydrous melts, J. Geophys. Res. 110 (2005), doi:10.1029/2004JB003215.

[37] D.M. Kerrick, G.K. Jacobs, A modified Redlich–Kwong equation for H_2O, CO_2, and H_2O–CO_2 mixtures at elevated pressures and temperatures, Am. J. Sci. 281 (1981) 735–767.

[38] H. Behrens, Y. Zhang, Ar diffusion in hydrous silicic melts: implications for volatile diffusion mechanisms and fractionation, Earth Planet. Sci. Lett. 192 (2001) 363–376.

[39] M. Nowak, D. Schreen, K. Spickenbom, Argon and CO_2 on the race track in silicate melts: a tool for the development of a CO_2 speciation and diffusion model, Geochim. Cosmochim. Acta 68 (2004) 512–5138.

[40] A.C. Rust, K.V. Cashman, Permeability of silicic magma: inertial and hysteresis effects, Earth Planet. Sci. Lett. 228 (2004) 93–107.

[41] C. Klug, K.V. Cashman, Permeability development in vesiculating magmas: implications for fragmentation, Bull. Volcanol. 58 (1996) 87–100.

[42] M.O. Saar, M. Manga, Permeability–porosity relationship in vesicular basalts, Geophys. Res. Lett. 26 (1999) 111–114.

[43] J.D. Blower, Factors controlling permeability–porosity relationships in magma, Bull. Volcanol. 63 (2001) 497–504.

[44] C. Klug, K.V. Cashman, C.R. Bacon, Structure and physical characteristics of pumice from the climactic eruption of Mount Mazama (Crater Lake), Oregon, Bull. Volcanol. 64 (2002) 486–501.

[45] S. Takeuchi, S. Nakashima, A. Tomiya, H. Shinohara, Experimental constraints on the low gas permeability of vesicular magma during decompression, Geophys. Res. Lett. 32 (2005), doi:10.1029/2005GL022491.

[46] C. Klug, K.V. Cashman, Vesiculation of May 18, 1980 Mount St. Helens magma, Geology 22 (1994) 468–472.

[47] A. Toramaru, Numerical study of nucleation and growth of bubbles in viscous magmas, J. Geophys. Res. 100 (1995) 1913–1931.

[48] C.C. Mourtada-Bonnefoi, D. Laporte, Kinetics of bubble nucleation in a rhyolitic melt: and experimental study of the effect of ascent rate, Earth Planet. Sci. Lett. 218 (2004) 521–537.

[49] H. Massol, T. Koyaguchi, The effect of magma flow on nucleation of gas bubbles in a volcanic conduit, J. Volcanol. Geotherm. Res. 143 (2005) 69–88.

[50] M. Mangan, T. Sisson, Delayed, disequilibrium degassing in rhyolite magma: decompression experiments and implications for explosive volcanism, Earth Planet. Sci. Lett. 183 (2000) 441–455.

[51] A. Burgisser, J.E. Gardner, Experimental constraints on degassing and permeability in volcanic conduit flow, Bull. Volcanol. 67 (2005) 42–56.

[52] C.D. Miller, Holocene eruptions at the Inyo volcanic chain, California: implications for possible eruptions in Long Valley Caldera, Geology 13 (1985) 14–17.

[53] K. Sieh, M. Bursik, Most recent eruption of the Mono Craters, eastern central California, J. Geophys. Res. 91 (1986) 12539–12571.

[54] M. Bursik, Subplinian eruption mechanisms inferred from volatile and clast dispersal data, J. Volcanol. Geotherm. Res. 57 (1993) 57–70.

[55] J. Castro, M. Manga, M.C. Martin, Slow vesiculation of obsidian domes inferred from H_2O concentration profiles, Geophys. Res. Lett. (submitted for publication).

[56] D.E. Sampson, Textural heterogeneities and vent area structures in the 600-year-old lavas of the Inyo volcanic chain, eastern California, Spec. Pap. Geol. Soc. Am. 212 (1987) 89–101.

[57] G. Heiken, K. Wohletz, Tephra deposits associated with silicic domes and lava flows, Geol. Soc. Am., Spec. Pap. 212 (1987) 55–76.

[58] N.W. Dunbar, P.R. Kyle, Volatile contents of obsidian clasts in tephra from the Taupo Volcanic Zone, New Zealand: implications to eruptive processes, J. Volcanol. Geotherm. Res. 49 (1992) 127–145.

[59] H.M. Gonnermann, M. Manga, Flow banding in obsidian: a record of evolving textural heterogeneity during magma deformation, Earth Planet. Sci. Lett. 236 (2005) 135–147.

[60] G.J.S. Bluth, W.I. Rose, Observations of eruptive activity at Santiaguito Volcano, Guatemala, J. Volcanol. Geotherm. Res. 136 (2004) 297–302.

[61] A. Goto, A new model for volcanic earthquake at Unzen Volcano: melt rupture model, Geophys. Res. Lett. 26 (1999) 2541–2544.